Ultra fast imaging NMR method for measuring fast transport processes in thin porous media

Magnetic Resonance Imaging 103 (2023) 61–74

Contents lists available at ScienceDirect

Magnetic Resonance Imaging

journal homepage: www.elsevier.com/locate/mri

Ultra Fast Imaging NMR method for measuring fast transport processes in thin porous media

R.J.K. Nicasy [a,d], H.P. Huinink [a,d,e,*], S.J.F. Erich [a,b,d], O.C.G. Adan [b], N. Tomozeiu [c,d,f]

[a] Eindhoven University of Technology, Applied Physics Department, P.O. Box 513, Eindhoven, 5600 MB, the Netherlands
[b] Organization of Applied Scientific Research, TNO, P.O. Box 49, Delft, 2600 AA, the Netherlands
[c] Canon Production Printing, Research and Development, AM department, Venlo, the Netherlands
[d] Transport in Permeable Media group, Department of Applied Physics, Eindhoven University of Technology, PO Box 513, Eindhoven 5600 MB, the Netherlands
[e] TNO Materials Solution, High Tech Campus 25, Eindhoven, the Netherlands
[f] Eindhoven Institute of Renewable Energy Systems, Eindhoven University of Technology, PO Box 513, Eindhoven 5600 MB, the Netherlands

ARTICLE INFO

Keywords:
GARField
Capillary penetration
T_1-relaxation
T_2-relaxation
Gadolinium (clariscan)
CuSO4

ABSTRACT

Measuring moisture distributions during fast transport processes in thin porous media is a challenging task. In this paper, Ultra Fast Imaging (UFI) NMR is proposed as a valuable measurement technique for investigating moisture uptake in porous media by achieving a temporal resolution of 10 ms and spatial resolution between 14.5 and 18 μm. This paper gives a detailed explanation about the methodology and the interpretation of the signal intensity. It is shown that there exist specific T_1- and T_2- relaxation time conditions for performing UFI experiments with signal-to-noise ratios that are sufficiently high. In most cases, a contrast agent is required to optimize these relaxation times and achieve the optimal measurement conditions. In the first part of this paper, both CuSO4 and Clariscan are discussed as possible contrast agents. Furthermore, it is shown that the signal intensity can be linked to the moisture content for water based liquids. The second part of this paper covers penetration experiments on porous PVDF membranes. These measurements show that the technique is able to measure moisture profiles during fast capillary penetration and allows to extract moisture front positions. Those front positions follow a linear time behavior in PVDF membranes. Lastly the NMR-measurements showed similar results when compared to scanning absorptometry (ASA).

1. Introduction

The absorption of liquids in porous substrates is an everyday phenomenon and crucial for applications such as paper-based microfluidics [1–3], printing [4–6], coatings [7,8], towels or tissues [9,10] and cooling of micro-electronics [11,12]. The rapid growth of these technologies demand a better understanding of the physical mechanisms that influence the fluid flow. In most cases, liquid absorption is driven by the capillary pressure, in which case the liquid uptake can be described by models such as Lucas-Washburn's [13] and Darcy's law [14]. However, experimental data revealed deviations from these theoretical models [15,16]. In the past decades, a wide variety of studies was performed towards the applicability of these laws for different porous systems with varying time and length scales leading to refinements of the models. Especially in the last few years much research was conducted on the usage of paper due to its availability, user-friendly, low cost and disposability [17–19]. However, experimental verification during capillary uptake is challenging for a few reasons. Firstly, in case of fast capillary uptake the time scales of interest often go below 1 s. Secondly, in the case of paper sheets or membrane filters, the thicknesses of around 100 μm form a challenge. Therefore, the measurement techniques should have a sufficient spatial and temporal resolution to cope with this.

Some measurement methods that were used for measuring droplet absorption are ultrasonic liquid penetration measurements (ULP) [4,5], contact angle measurements (CA), automatic scanning absorptometry (ASA) [20] or high speed cameras [21]. All these techniques meet the temporal resolution but measure only parameters with global information about the droplet absorption. To gain information about the liquid distribution inside the porous media, assumptions about the movement of liquid have to be made. There have been efforts to interpret the global information obtained with these techniques into characteristics of the

* Corresponding author at: Eindhoven University of Technology, Applied Physics Department, P.O. Box 513, Eindhoven, 5600 MB, the Netherlands.
E-mail address: h.p.huinink@tue.nl (H.P. Huinink).

https://doi.org/10.1016/j.mri.2023.06.009
Received 16 February 2023; Received in revised form 1 June 2023; Accepted 17 June 2023
Available online 20 June 2023

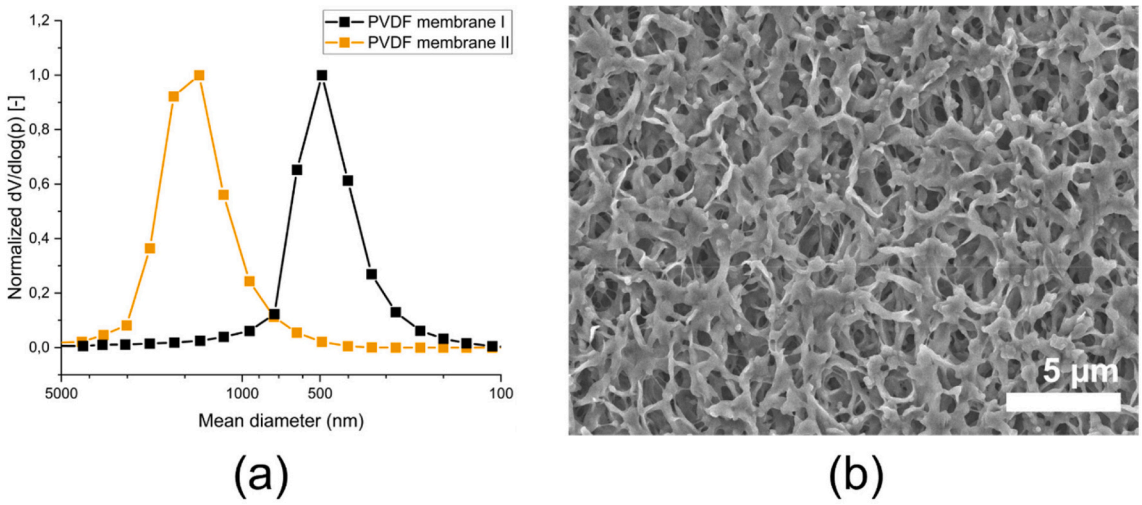

Fig. 1. (a) pore size distributions for PVDF membrane I (black) and PVDF membrane II (orange) measured by MIP. (b) SEM image of the top side of PVDF membrane I.

Table 1
The liquids used in this study and their physical properties.

	Contrast agent (M)	Glycerol (wt%)	Viscosity (mPa.s)	Surface tension (mN/m)
$CuSO_4$ based liquids	0.1	0	0.89	72.3
	0.1	25	1.89	70.7
	0.1	50	5.38	68.5
	0.1	70	20	66.1
Clariscan based liquids	0.048	0	1.09	67.3
	0.016	25	2.18	66.46
	0.008	50	6.24	64.9
	0.007	70	24.10	62.95

fluid redistribution inside paper: i.e. the location of the absorption front or the liquid distribution. However, interpreting the global information in a correct manner becomes difficult in complex systems, such as printing paper, where effects like hydrophobicity, swelling or film flow will affect the liquid penetration in ways that are still not completely understood [22].

In these complex systems, direct measurement of the moisture content with sufficiently high spatial and temporal resolution could identify physical phenomena such as fingering, film flow, changeable pore sizes and filling of intra-fibres pores [22]. This would allow to study hydrophobic, inhomogenious or swellable porous media in which the liquid uptake is much more complex and still challenging to investigate.

A promising technique to measure liquid distribution in porous media is Nuclear Magnetic Resonance (NMR). In previous studies, NMR was used to measure the penetration of water-glycerol mixtures in Al2O3 [23] or ink in paper [24]. Despite the promising results, conventional NMR systems are still unable to meet the high spatial- and temporal-resolution required to measure fast liquid uptake in thin porous media. In order to gain more spatial resolution, high-gradient NMR-setups are designed. Promising measurements were performed with an NMR-MOUSE by Mohebbi et al. [25,26]. In this study, 1D-liquid profiles in stacked layers with a total thickness of 600 µm were measured with a spatial resolution of 25 µm and temporal resolution of 0.2 s. Another high-gradient setup is the GARField NMR, introduced by Glover [27]. The GARField NMR can achieve very high gradients due to its uniquely designed magnetic poles leading to resolutions as high as 5 µm [28]. Unfortunately, measuring liquid redistribution inside porous layers of about 100 µm (i.e. single paper sheets) demands for temporal resolutions of a several milliseconds as liquid uptake occurs within 0.1 s [4]. Recently, it was demonstrated that by using a combination of the GARField setup and an ultra fast imaging (UFI) method, it is possible to measure in real time, the fluid distribution in thin porous media with a resolution of 14.5–18 µm and a minimum time resolution of 10 ms [29]. The technique was used to measure the liquid distributions in Nylon 6,6 membranes during droplet penetration. The liquid profiles could be used to demonstrate that the liquid front scaled with pore radii, viscosity and surface tension as predicted by Darcy's law. The newly introduced NMR technique showed promising results and provides good potential for investigation physical phenomena in complex porous media: especially in the pulp-paper industry, where due to its complex nature the liquid penetration inside paper is still not fully understood.

In the previous study, the potential of the technique was highlighted but only limited information was given about the measurement techniques itself. This article provides an in-depth discussion of the ultra fast imaging (UFI) NMR technique, explaining the setup, pulse sequence and signal optimization. The goal of the given technique is to gain crucial information on the penetration of complex liquids penetrating in thin porous media.

The article will start by explaining the GARField NMR setup followed by a theoretical analysis of the signal intensity that is measured with the UFI-NMR method. In the results section, the usage of contrast agent to optimize the signal intensity is demonstrated. Finally, liquid distribution measurements during uptake in PVDF membranes are discussed, which are compared with ASA - measurements.

2. Materials & methods

2.1. Membrane samples

The membranes used in this study are hydrophilic polyvinylidene fluoride (PVDF) membrane filters produced by Durapore with a thickness of 110 µm. The porosity of the PVDF membrane filters are 65%. Pore size distributions of the membranes are measured with mercury intrusion porosometry (MIP), see Fig. 1a. The mean pore diameter is 0.46 µm for PVDF membrane I and 1.4 µm for PVDF membrane II. A scanning electron microscopy (SEM) image of the top surface of PVDF membranes I is shown in Fig. 1b. Samples are prepared by taking 18 by 18 mm pieces out of the membranes filters and fixate them on top of a glass cover slip with double sided tape.

2.2. Liquid solutions

The liquid solutions used in this study are shown in Table 1. The solutions are made by mixing demineralized water type 1, glycerol and

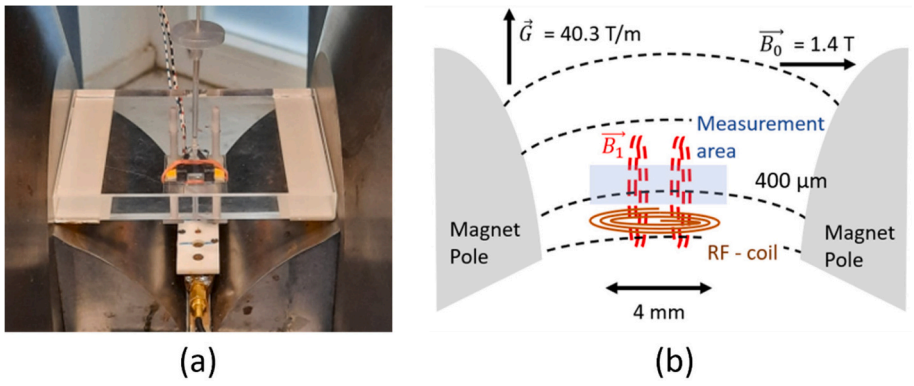

Fig. 2. a: Picture of the NMR-setup and droplet insert. b: Schematic representation of the NMR-setup.

in case of the NMR-experiments a watery solution containing either Clariscan or CuSO4. The glycerol (> 99.0% purity) has a density of 1.26 g/cm^3 and is used to tune the viscosity of the liquid solutions.

Clariscan (C16H25GdN4O8) and CuSO4 are both contrast agents that are added to manipulate the NMR-characteristics of the solution. CuSO4 (99,7% purity) is provided by Merck in powder form and Clariscan is a Gadolinium based contrast agent used in medical MRI [30]. The Clariscan is provided in a water like solution with a concentration of 279.3 g/ml, which is equivalent to 0.5 mmol/ml. It has a pH between 6.5 and 8, a density of 1.349 g/ml and a viscosity of 3.0 mPa.s at room temperature [31].

Viscosity and surface tension for the CuSO4 solutions are taken from literature [32]. For the Clariscan solutions, the viscosities are measured with an Anton Paar MCR302 rheometer (20 °C) while the surface tension are determined using the pendant drop method [33]. The surface tension for the Clariscan solutions are 5–7% lower than the once found for a pure water-glycerol mixture. This is however due to a systematic error within the pendant drop method, because pure water-glycerol mixtures gave the same lower values.

2.3. Automatic scanning absorptometer

The Automatic Scanning Absorptometer (ASA) [34] is a device that is similar to the more know Bristow wheel [35]. The ASA setup used in these experiments is the Kumagai Riki Kogyo (KM 500 win). The device is able to measure the absorbed liquid on timescales ranging from 10 ms to 10 s. ASA setup uses a spiral-scan device, meaning that the tracks that are made are spiral in nature.

In the experiment, a glass capillary is filled with the desired liquid followed by the fixation of the porous sample on a turntable. Thereafter, the liquid within the glass capillary will be brought in contact with the porous sample by using a scanning head. Due to capillary forces, the liquid starts to penetrate inside the membrane and is drown out of the glass capillary. During the measurement, a sensor will track the movement of the liquid as meniscus in the glass capillary. This sensor movement together with the inner diameter of the glass capillary are then used to calculate the transferred liquid (TLV), which has penetrated in a specific area ($A[m^2]$) during a specific contact time ($t(s)$). By accelerating the turntable, the time can be varied between 10 ms and 10 s. The area of absorption (A) is equal to the dimensions of the nozzle which in this research had a width of 1 mm and a length of 5 mm. The same nozzle is used for all experiments.

3. Ultra Fast Imaging (UFI) method for fast high-resolution 1D imaging

NMR (Nuclear Magnetic Resonance) imaging can be used for measuring liquid distributions in porous media. In this section the theory and setup behind the UFI method is introduced. First, the theoretical basis to measure 1D-liquid profiles using NMR is discussed. Second, the GARField-NMR is introduced and thirdly, the signal intensity and method behind UFI are explained.

3.1. Basic theory

NMR can be used to image nuclear spins and therefore ^{1}H atoms. Before a signal can be recorded, the spins are aligned using a static magnetic field with magnitude $B_0[T]$, which by convention points into the z-direction. Besides the main magnetic field, a magnetic gradient $G[T/m]$ is used to encode spatial information. Spins that experience a magnetic field $B[T]$ will resonate at a typical frequency, $f[Hz]$, determined by the magnitude of the magnetic field and the magnetic gradient according to:

$$f(x) = \frac{\gamma}{2\pi}(B_0 + Gx) \tag{1}$$

where $f[MHz]$ is the Larmor frequency and $\gamma[rad.MHz/T]$ is the gyromagnetic ratio, which for hydrogen is 267.40 $rad.MHz/T$ and $x[m]$ the position of the atoms. By using a Fourier transformation, the different frequencies can be extracted which provides information about the local moisture content in space. Signal is generated by exciting the atoms with a radio frequency (RF) pulse send by an RF-coil. The same RF-coil is also used to measure the NMR-signal. Directly after excitation, the spins start to relaxate back to their equilibrium due to spin-spin or T_2-relaxation and spin-lattice or T_1- relaxation with characteristics timescales $T_2[s]$ and $T_1[s]$. The final signal intensity is proportional to the density of hydrogen atoms $\rho[kg/m^3]$ and can be expressed by,

$$S \propto \rho\left[1 - exp\left(-\frac{t_r}{T_1}\right)\right] exp\left(-\frac{t_e}{T_2}\right), \tag{2}$$

where $t_r[s]$ is the repetition time and $t_e[s]$ is the echo time, both pulse sequence parameters set by the user.

3.2. GARField NMR

The NMR-setup used in this research is based on the GARField method, which was introduced by Glover et al. [27]. This is one of the few NMR designs that is capable off imaging the moisture profile in thin layers with sufficient spatial resolution. A detailed review about the ability and working of this NMR-setup is given by Nicasy et al. [28]. Here, we only give the necessary information required to understand the working of UFI-method. A picture and schematic representation of the setup are shown in Fig. 2. The main difference between the GARField NMR and a conventional NMR-setup are the special designed magnetic poles [36,37]. The poles have a curved shape that can be seen in Fig. 2. Because of these poles, the gradient of the GARField NMR can go up to 44 T/m. Because spatial encoding is directly linked to the gradient

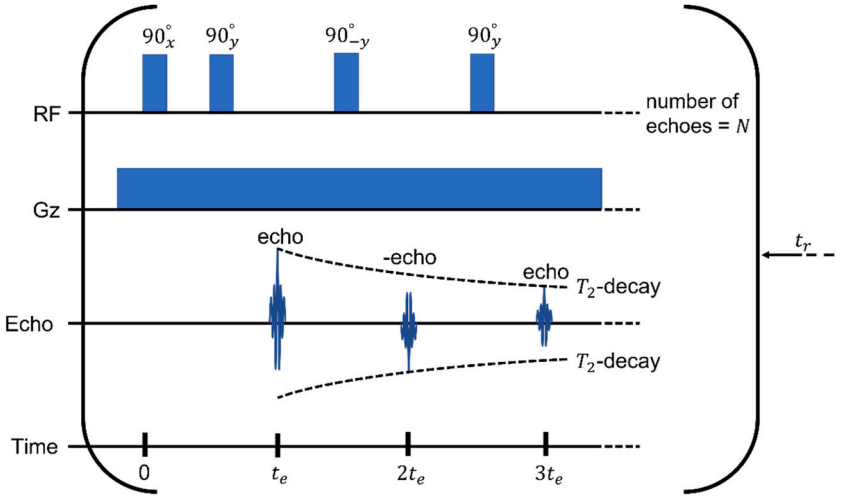

Fig. 3. Schematic representation of the UFI - pulse sequence.

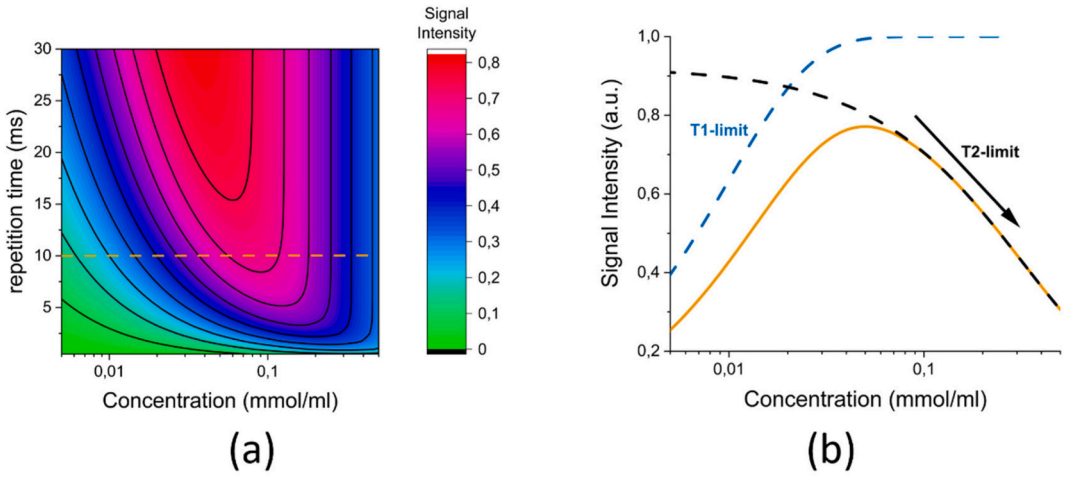

Fig. 4. a: Contour plot showing the theoretical signal intensity in function of the repetition time (ms) and concentration of contrast agent (mmol/ml) for a fictive contrast agent having the following relaxation characteristics: $1/T_2 = 1/0.010 + 3500C$ and $1/T_1 = 1/3 + 3200C$. b: Signal intensity in function of contrast agent concentration for a repetition time of 10 ms, which corresponds to the orange line in figure a. Shown in dotted blue and black lines are the T_1- and T_2- factor found in eq. (4).

(eq.1), the achievable resolution of the GARField setup is much higher than in case of conventional NMR systems. Commonly reported resolutions are between 5 and 15 μm [28]. The maximum theoretical resolution (Δr) that can be achieved is given by:

$$\Delta r = \frac{1}{\gamma G_x \Delta t_a}, \tag{3}$$

with $G_x[T/m]$ the gradient and $\Delta t_a[s]$ the acquisition time. Typical values for G_x and Δt_a are 40 T/m and 50 μs which results in a theoretical resolution of 11.7 μm. Because both G_x and γ are fixed, increasing the resolution can only be achieved by increasing Δt_a. However increasing Δt_a will lead to more relaxation and a drop of the signal-to-noise ratio.

Excitation of the hydrogen atoms and recording the signal intensity is done by an RF-coil. A signal profile is measured using a single pulse sequence in the presence of a constant gradient. Afterwards, a Fourier transform of the echo is used to build up a signal profile [38]. The RF-coil is located as close as possible to the measurement area to have the highest possible signal-to-noise ratio. A drawback of this design is a decrease in signal intensity when moving away from the RF-coil. This leads to a coil-profile and a limitation in the maximum Field-Of-View (FOV) that can be achieved with the NMR-setup. The FOV in these experiments is typically limited to 400 μm.

To jet droplets on top of the samples, a syringe is used, shown in Fig. 2a. After ejection, the droplet is detected by an Omron droplet sensor type EE-SX3070. The sensor is connected via an Arduino to the NMR setup which triggers the measurement when a droplet is detected.

3.3. Pulse sequences

- Saturation recovery (T_1-time)

Measurements of the T_1-relaxation time are performed by a saturation recovery sequence given by: $\left[\alpha_y^\circ - \tau_1\right]_m - \tau_2 - 90_x^\circ - \tau - 90_y^\circ - \text{echo}$, where m denotes the amount of saturation pulses and α represents the flip angle [28,39].

- Ostroff-Waugh (T_2-time)

Measurements of the T_2-relaxation times are performed by an Ostroff-Waugh (OW) [28,40] sequence given by $\left(\alpha_x^\circ - \tau - \left[\alpha_y^\circ - \tau - \text{echo} - \tau\right]_N\right)$, where N denotes the amount of

Table 2
NMR-relaxation properties of Clariscan and CuSO4 in different water-glycerol mixtures, found in eq. 6 and 7. T2bulk and T1bulk are the relaxation times for pure water-glycerol mixture (no contrast agent added).

	Glycerol (wt%)	T_{2bulk} (ms)	T_{1bulk} (ms)	R_2 (ms^{-1} M^{-1})	R_1 (ms^{-1} M^{-1})
Clariscan	0	10.7	2480	5.13 ± 0.54	4.48 ± 0.32
Based liquids	25	15.00	1480	9.29 ± 0.34	7.66 ± 0.16
	50	22.9	980	17.10 ± 1.15	23.52 ± 1.34
	70	31.9	300	46.34 ± 0.54	34.35 ± 1.65
$CuSO_4$ based	0	10.7	2480	0.74 ± 0.03	0.62 ± 0.02
liquids	25	15.00	1480	1.25 ± 0.04	0.99 ± 0.03
	50	22.9	980	2.91 ± 0.10	1.91 ± 0.18
	70	31.9	300	5.34 ± 0.08	4.16 ± 0.17

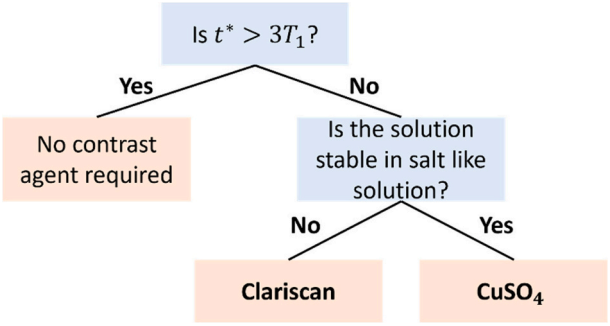

Fig. 5. Decision Tree for deciding which contrast agent should be used.

echoes that are measured and α represents the flip angle. In this research, the OW sequence is used instead of the more frequently used CPMG sequence because of the constant flip angles in the OW sequence. A CPMG will use both 90° and 180° pulses. Because the excitation profiles depends on the pulse type [41], it is preferred to use only one pulse angle and ensure a constant excitation profile.

- Fast Pulse Sequence (Signal Intensity)

To measure liquid distributions with sufficient temporal resolution, our method combines two main ingredients: summation of the echoes which ensures a rapid increase in the signal-to-noise ratio and shortening of the T_1-relaxation time of the solution by adding a contrast agent. Both the echo summation and the shortening of the T_1-relaxation time will be discussed in more detail in this section.

The signal intensity during fast liquid uptake is measured with an adaptation of the OW-pulse sequence [40], and is given by, $90^{\circ}_{x} - \tau - \left[90^{\circ}_{y} - \tau - (\text{echo}) - \tau - 90^{\circ}_{-y} - \tau - (-\text{echo}) - \tau\right]_N$, where N is the amount of repetitions within one measurement. A schematic representation of the pulse sequence is given in Fig. 3. The difference compared to the OW-sequence is alternating between positive (90°_{y}) and negative (90°_{-y}) flip angles, instead of only using positive flip angles. Consequently, positive and negative echoes will be created in alternating fashion.

The final signal intensity is calculated by adding all N positive echoes together with the negatives of the N negative echoes. Because the signal is measured in one single measurement, in the presence of a constant gradient, a Fourier transformation is required to transfer the signal intensity to signal profiles. The reason for adding up the different echoes is to have a fast increase in S/N-ratio while flipping the echoes ensures that after addition, the constant background noise is cancelled. The downside of doing a summation over all echoes is that the measured profiles will become T_2-weighted. In a CPMG measurement, the different echoes can be used to discriminate between multiple T_2-times, which provides information about multiple hydrogen pools. This becomes impossible within our UFI-measurement.

The intensity of one echo is given by eq. (2). Therefore, the total signal intensity can be written like:

$$S = \rho\left(1 - exp\left(-\frac{t_r}{T_1}\right)\right)\sum_{n=1}^{2N} exp\left(-n\frac{t_e}{T_2}\right). \tag{4}$$

This equation is a geometric series and can be rewriting into:

$$S = \rho\left(1 - e^{-\frac{t_r}{T_1}}\right)\left[\frac{e^{-\frac{t_e}{T_2}} - e^{-(2N+1)\frac{t_e}{T_2}}}{1 - e^{-\frac{t_e}{T_2}}}\right]. \tag{5}$$

A detailed derivation of eq. (5) can be found in Appendix A.

In our experiments N was set to 16 leading to the summation of 32 echoes (16 positive and 16 negative echoes). In this study, the pulse length (t_{90}) was equal to 1 μs and the echo time ($t_e = 2\tau$) was equal to 50 μs leading to a measurement time (t_p) of 1.6 ms for one moisture profile.

Before a next profile can be measured, the hydrogen nuclei need to relax back to their equilibrium condition, where the repetition time (t_r)

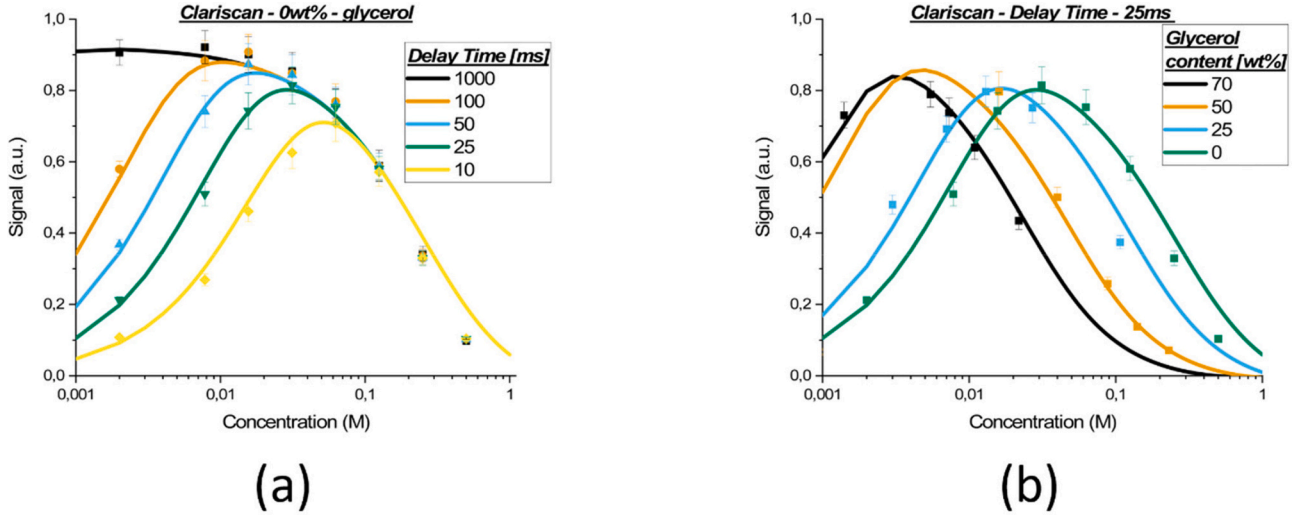

Fig. 6. a: Comparison between the signal intensity predicted based on the relaxation characteristics of a clariscal solution of 0 wt% glycerol (lines) and measurements by UFI (points) Both are given for different repetition times. b: Same graph but for different water-glycerol concentration, with the same long repetition time of 25 ms.

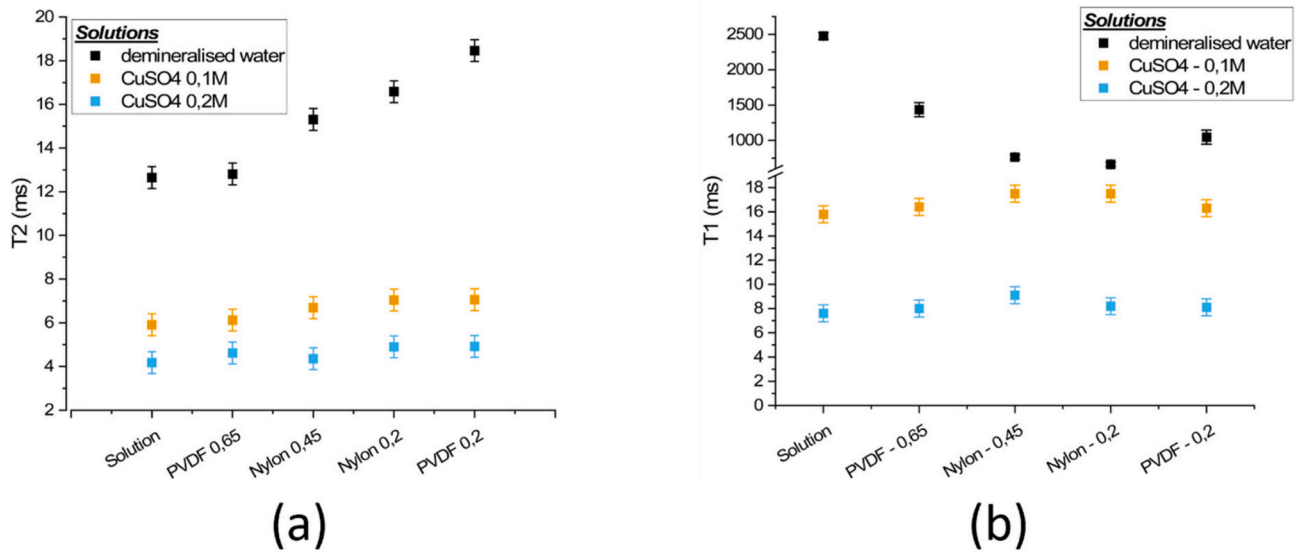

Fig. 7. a: T_2-relaxation data measured in different porous media for demi water (black), CuSO4 solution 0.1 M (orange) and CuSO4 solution 0.2 M (blue). b: T_1-relaxation data measured in different porous media for demi water (black), CuSO4 0.1 M (orange) and CuSO4 0.2 M (black).

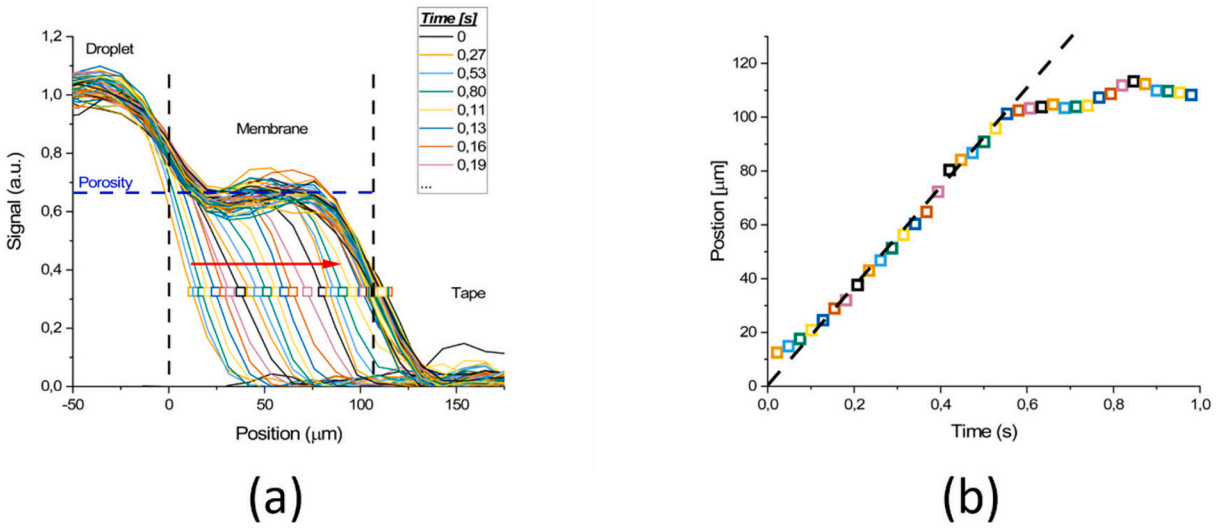

Fig. 8. *a: Moisture profiles measured during penetration of a Clariscan based mixture containing 50 wt% - glycerol in a PVDF membrane with pore size 0.22* µm. *b: Front* versus *t* graph for the liquid profiles shown in a.

should be $t_r > 3T_1$. This condition is chosen instead of the more frequently used condition $t_r > 5T_1$, because waiting an extra $2T_1$ would only increase the signal intensity from 95% to 99% but almost doubles the measurement time. Because in our case measurement time is the most important factor, the first condition is chosen. The time between two profiles is therefore $t_m = 3T_1 + t_p = 3T_1 + 1.6\text{ms}$.

From eq. (4), it becomes clear that in order to do fast imaging, a low T_1 and long T_2 are required. When profiles are required for example every 25 ms, the signal intensity of normal water ($T_1 = 3$ s) will reduce to zero because of a T_1-factor of 0.0083. Therefore, no signal can be measured using normal water, similar to most liquids. To solve the problem of signal loss, an NMR-contrast agent is added to decrease the T_1-time to meet the condition $t_r \geq 3T_1$ which ensures a 95% signal recovery. A second condition for the T_2-time should ensure that the signal intensity of the N_{th} - echo is still high-enough to be measured. For simplicity, a signal intensity of 37% is chosen, leading to the condition: $Nt_e \geq T_2$.

Measurement conditions:

- time between profiles $= t_r \geq 3T_1$
- time to measure one profile $= Nt_e \geq T_2$

This results in a measurement time of $t_m = t_r + Nt_e \approx 3T_1 + T_2$. To find the optimum signal intensity, the impact of the concentration of contrast agent should be investigated, this is discussed in the following sections.

3.4. Signal characterization and calibration

In this section, a better understanding of the signal intensity and the corresponding signal optimum is given. Because the signal intensity is T_2- weighted and the T_1-condition ($t_r \geq 3T_1$) cannot always be simultaneously fulfilled, the resulting signal intensity is a function of concentration of contrast agent. Our first step is a theoretical discussion on the effect of a contrast agent on the signal intensity measured with the UFI method. In section 4, a comparison will be made with experiments.

In order to control the T_1- and T_2-relaxation time, contrast agents are used. The effect of a contrast agent on both relaxation times is given by

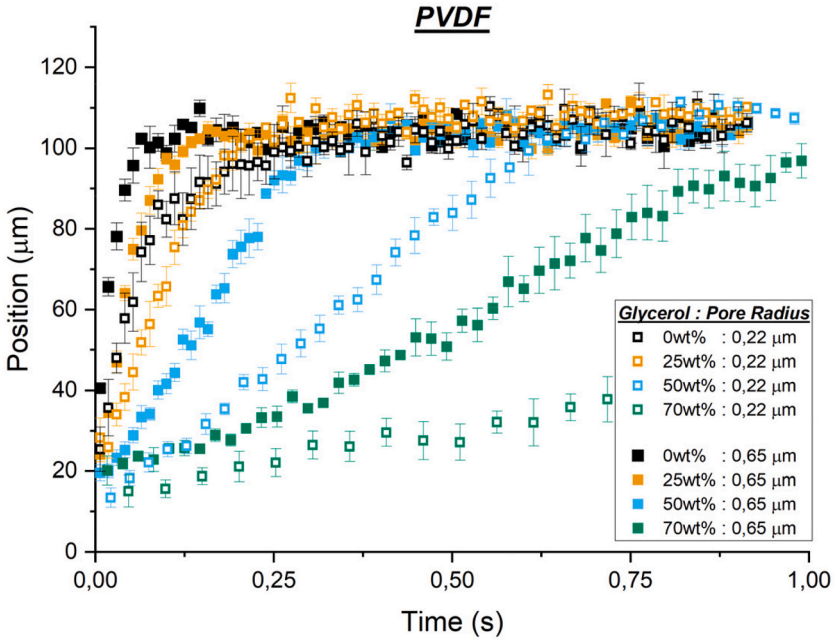

Fig. 9. Liquid front positions in function of time measured for the different Clariscan based water-glycerol mixtures of Table 1 containing 0, 25, 50 and 70 wt% of glycerol on two different PVDF membranes with pore radius of 0.22 and 0.65 µm.

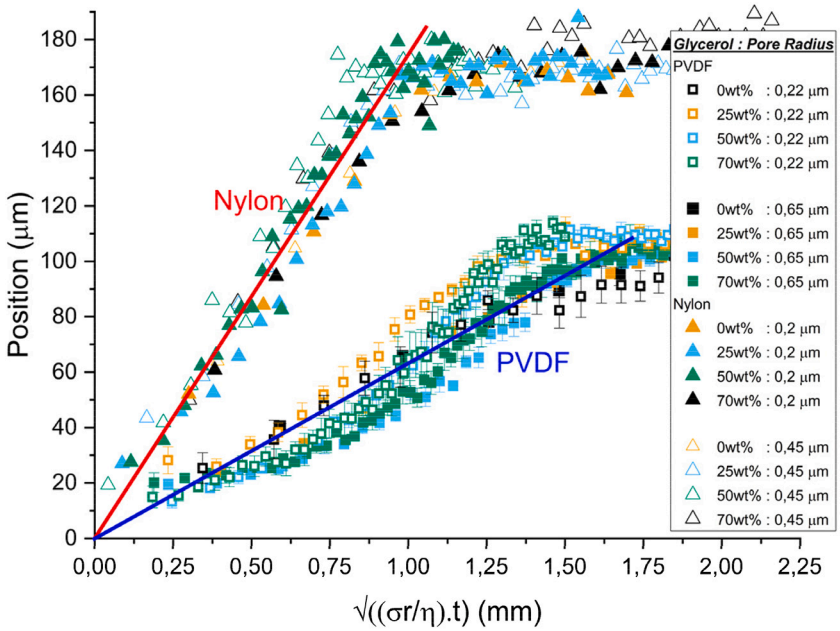

Fig. 10. Liquid front positions in function of $\sqrt{\sigma r t/\eta}$ for different water-glycerol mixtures containing 0, 25, 50 and 70 wt% of glycerol on two different PVDF membranes (pore radius of 0.22 and 0.65 µm) and two different Nylon membranes (pore radius of 0.2 and 0.45 µm), where the later data is taken from Nicasy et al. [29].

[42]:

$$\frac{1}{T_2} = \frac{1}{T_{2bulk}} + R_2 C, \tag{6}$$

$$\frac{1}{T_1} = \frac{1}{T_{1bulk}} + R_1 C, \tag{7}$$

where $c[M]$ is the concentration of the contrast agent. The parameters $R_1\left[M^{-1}S^{-1}\right]$ and $R_2\left[M^{-1}S^{-1}\right]$ are the relaxivity of the contrast agents [43,44]. By implementing these relations in eq. (4), the signal intensity as a function of the contrast agent concentration is known. A closer look to this equation will help in selecting the best concentration of contrast agent to achieve the highest signal intensity. An experiment starts by selecting the proper repetition time (t_r) which determines the window between two measured liquid profile and depends on the speed of the physical process. Other parameters such as the ones found in eq. (6) and (7) are dependent on the type of contrast agent and can be found in Table 2 for Clariscan and CuSO4. Selecting the proper contrast agent will depend on the type of experiment that is performed and will be discussed at the end of this chapter.

For the theoretical discussion on the impact of a contrast agent on the

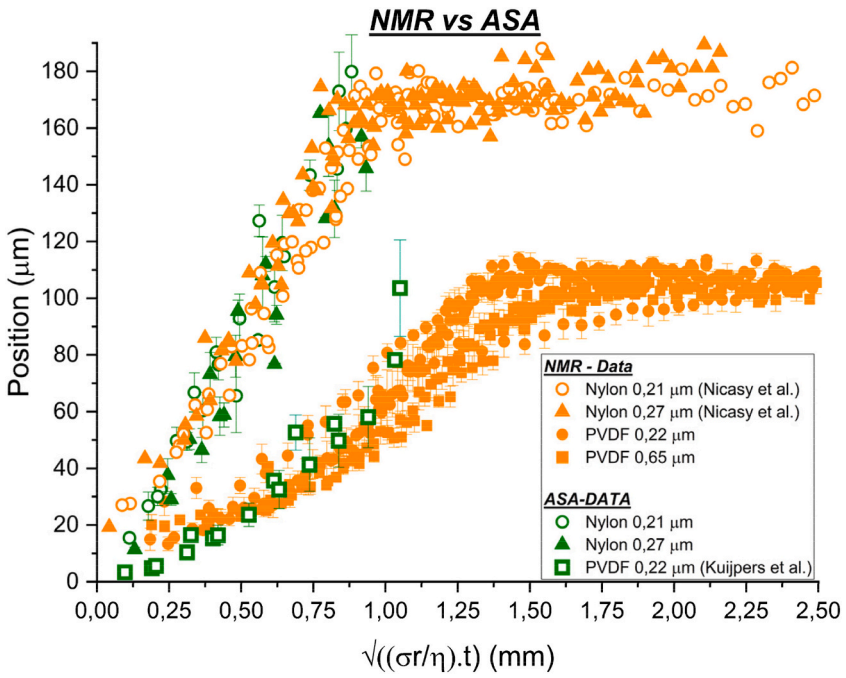

Fig. 11. Comparison between liquid front positions measured by ASA (green) and UFI (orange) on a rescaled time axis for PVDF- and Nylon-membranes. For every membrane and technique, the data for all glycerol contents (0, 25, 50 and 70 wt%) is shown in similar symbols. (For interpretation of the references to colour in this figure legend, the reader is referred to the web version of this article.)

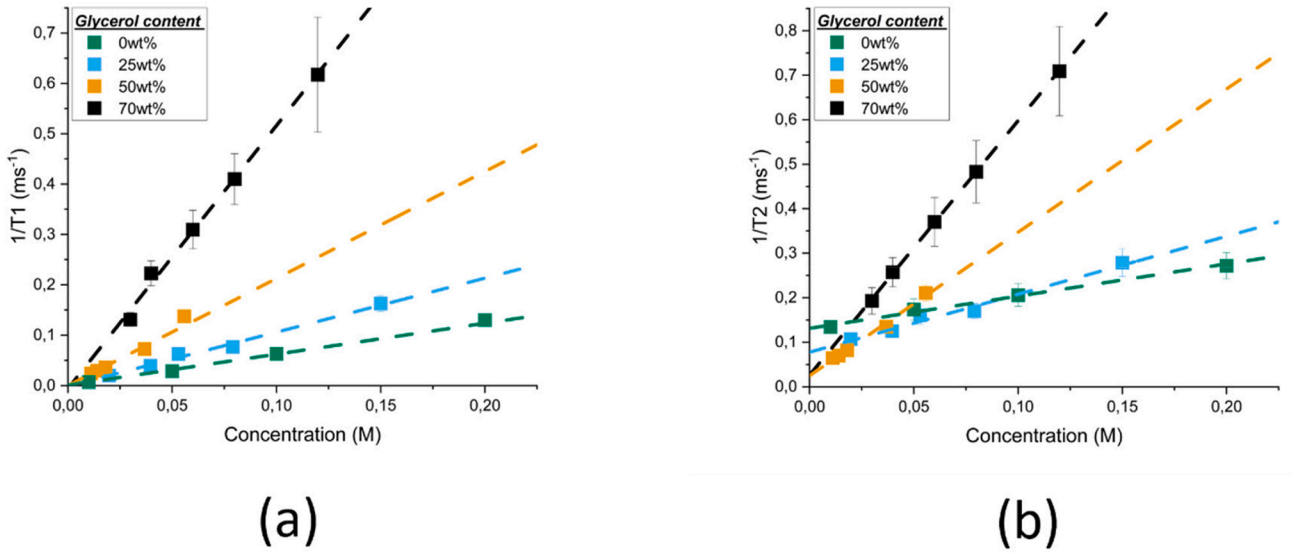

Fig. 12. Inverse T1- (a) and T2- (b) relaxation times in function of CuSO4 concentration for solutions containing a different water-glycerol ratio: 0 wt% (green), 25 wt% (blue), 50 wt% (orange) and 70 wt% (black). Relaxation times were measured by saturation recovery (T1) and OW-sequence (T2). (For interpretation of the references to colour in this figure legend, the reader is referred to the web version of this article.)

signal intensity, relaxivity rates for commonly used contrast agents are used: $R_1 = 3200\ M^{-1}\ s^{-1}$ and $R_2 = 3500\ M^{-1}\ s^{-1}$ [44]. T_{2bulk} and T_{1bulk} are set to 10 ms and 3 s respectively which are the values for water found within our GARField NMR-setup. Using these values in eq. (5), the signal intensity for different combinations of repetition time and concentration of contrast agent can be determined. Fig. 4 shows a contour plot of the signal intensity in function of both parameters. The figure shows that faster measurement times will lead to lower signal intensity and require more contrast agent to achieve the maximum achievable signal intensity.

To explain the occurrence of an optimum in the signal intensity for a specific concentration of contrast agent, a closer look is taken to the signal intensity for $t_r = 10$ ms, marked with an orange line in Fig. 4a. The signal intensity for different concentrations that corresponds with this repetition time can be seen in Fig. 4b. Fig. 4b also shows the T_1 (blue) and T_2 (black) contributions to the signal intensity. With increasing concentration of contrast agent, the signal first increases. This can be explained by an increase in the T_1-term found in eq. (4). By increasing the concentration of contrast agent and thus lowering the T_1-time, the T_1-condition imposed earlier ($t_r > 3T_1$) will become more and more fulfilled. When comparing the signal intensity to the T_1-term in blue, it can be seen that the signal at low concentrations is T_1-limited. From the

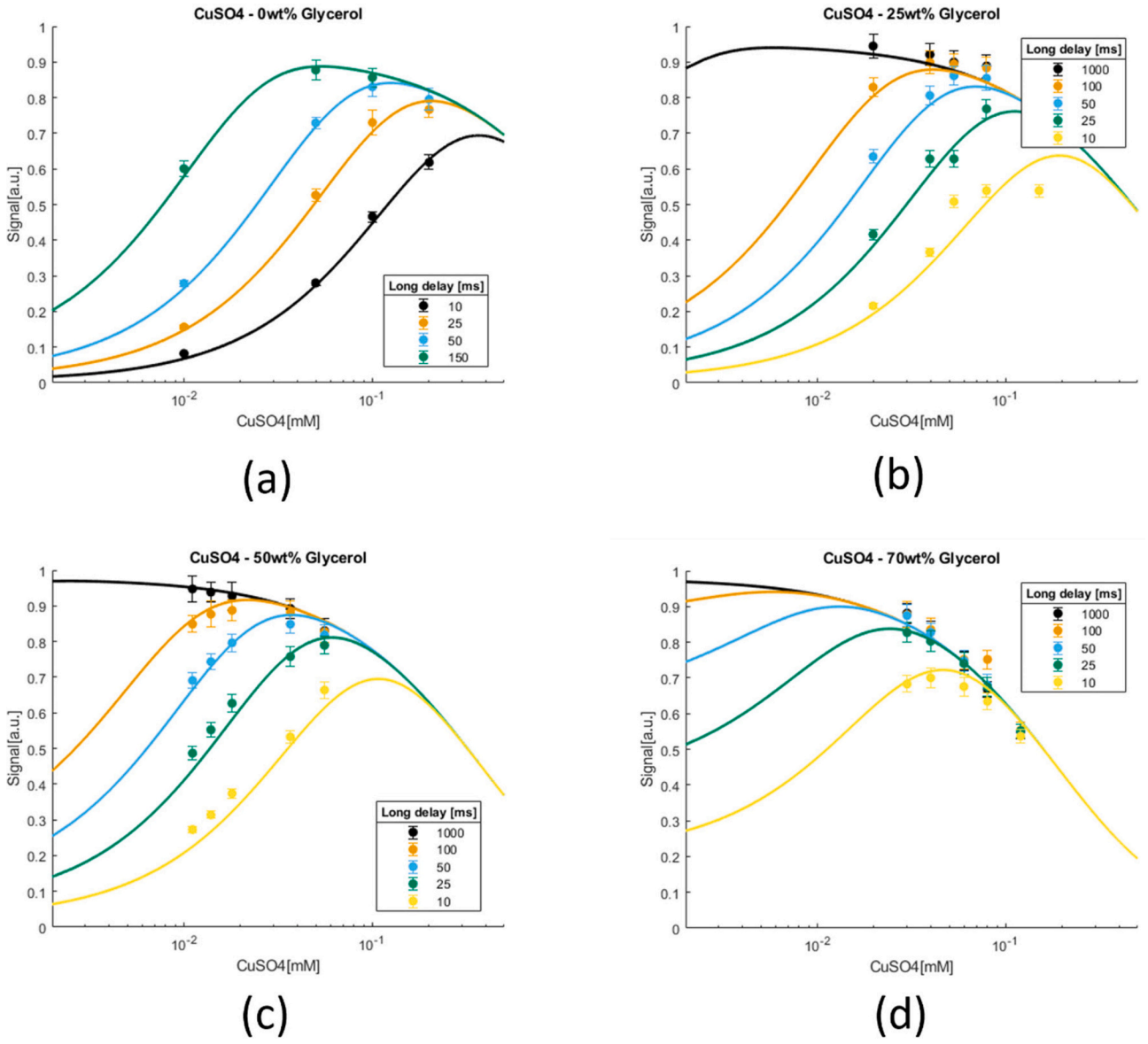

Fig. 13. Fast Sequence signal intensities data for $CuSO_4$ containing solutions predicted by the contrast agent relaxivities (lines) and experimental results (points). The figures show the values for different glycerol contents (0 wt% (a), 25 wt% (b), 50 wt% (c) and 70 wt% (d)) where in every graph the values are given for different delay times marked with varying colours.

moment the T_1-condition is met, which in this case is around 0.05 mmol/ml, 95% of the signal will be recovered. Besides lowering the T_1-time, increasing the amount of contrast also lowers the T_2-time, which explains why, at a certain concentration, the signal intensity starts to decrease again. These lower T_2-times lead to lower echo intensities resulting in a decrease in the T_2-term found in eq. (4), plotted in black in Fig. 4b. By comparing the total signal intensity with the T_2-term, it can be seen that the signal intensity is dominated by the T_2-effect at higher concentrations.

This simultaneous decrease in T_2- and T_1- time when increasing the contrast agent concentrations explains the optimum in the signal intensity. Therefore, the proper concentration of contrast agent should be determined for every liquid mixture in order to have the best Signal-to-Noise.

3.5. Selecting the right contrast agent

Preparing a solution for the NMR-experiment starts by identifying the typical timescale of the physical process $t^*[s]$ that want to be investigated and the T_1 time of the liquid solution. When the $t^* > 3T_1$, signal recovery is fast enough to ensure 95% signal intensity and no contrast agent is required. If $t^* < 3T_1$, initial signal recovery is to slow and contrast agents are required to decrease T_1.

In this project, two contrast agents were used, i.e. $CuSO_4$ and Clariscan. If the liquid is stable in a salt like environment, $CuSO_4$ is preferable because it has the smallest effect on viscosity and surface tension. However, in case the solution is unstable in a salt-like environment, the case for most colloidal systems, Clariscan will be used. Clariscan will slightly increase the viscosity, but, due to its inert nature, will not interfere with the particle stability and is therefore preferred.

3.6. Settings and NMR-parameters used in this study

The GARField setup in this study has a $G_x$of 40.3 T/m, a B_0 of 1.46 T which corresponds to a Larmor frequency of 60.5 MHz The best measurement conditions with respect to the S/N-ratio, measurement time and resolution was achieved with an echo time of 50 μs and an acquisition time of 40 μs which was kept constant throughout the

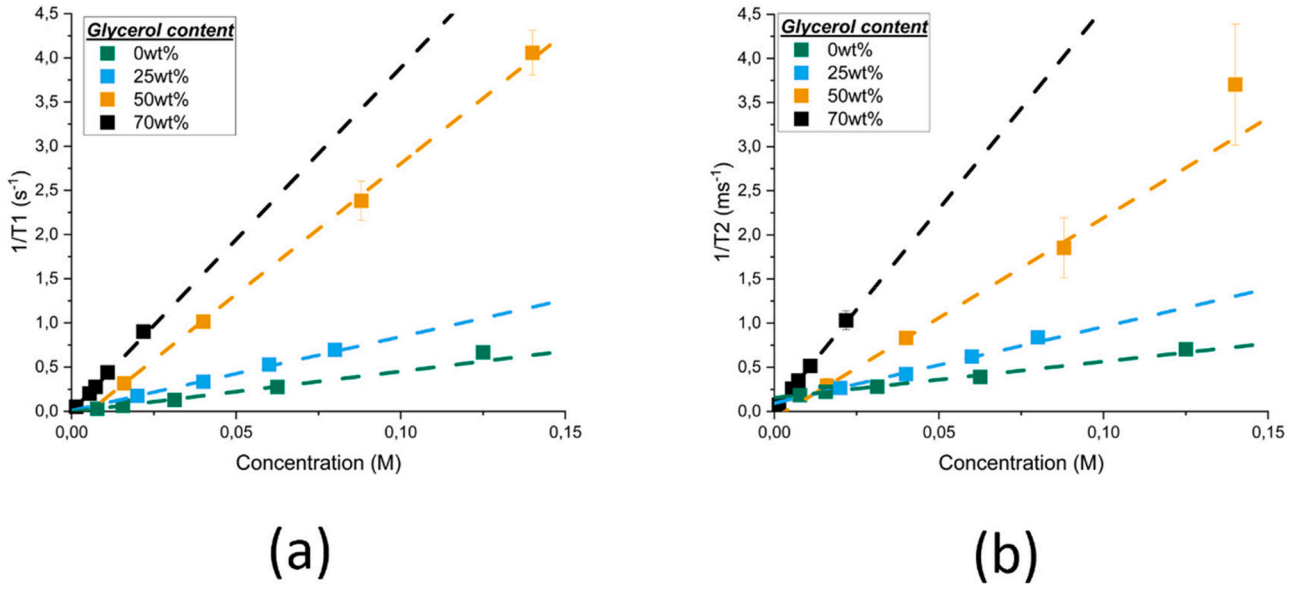

Fig. 14. Inverse T1- (a) and T2- (b) relaxation times in function of Clariscan concentration for solutions containing a different water-glycerol ratio: 0 wt% (green), 25 wt% (blue), 50 wt% (orange) and 70 wt% (black). Relaxation times were measured by saturation recovery (T1) and OW-sequence (T2). (For interpretation of the references to colour in this figure legend, the reader is referred to the web version of this article.)

experiments. These specific values resulted in a theoretical resolution of 14.5 μm. The experimentally determined spatial resolution is 18 μm, slightly higher than the theoretical resolution. The t_r was varied between 10 and 25 ms depending on the speed of penetration.

The RF-coil used in these experiments has a diameter of 4 mm which represents to the total measurement area. The measured signal intensity also depends on the distance with respect to the RF-coil. To correct for this coil-profile, all measurements are corrected with a $CuSO_4$ reference sample from which the proton density is known. A $CuSO_4$ solution is used instead of water, because of its shorter T_1-time and therefore shorter measurement time. The FOV of our setup was 300 μm.

4. Results

4.1. The relation between signal and contrast agent

In the previous section, the effect of a contrast agent on the signal intensity was explained theoretically. In this section, an experimental verification of eq. (4) will be given, by comparing UFI measurements of the signal intensity with predictions based on the T_1- and T_2-relaxation characteristics of the liquid. The comparison was performed for water-glycerol mixtures containing varying amounts of Clariscan and $CuSO_4$.

In the first part of the section, the relaxation characteristics of Clariscan and $CuSO_4$ within different water-glycerol mixtures are discussed. The data was determined with an OW-sequence ($t_e = 50$ μs, $t_r =$ 25 to 100 ms) and saturation recovery.

Table 2 gives the results for the different relaxation parameters in eqs. (6) and (7). The corresponding relaxation times as a function of concentration can be found in Appendix B, in Fig. 12 and Fig. 15. It was found that increasing the glycerol content will increase the relaxivity for both Clariscan and $CuSO_4$. This is in line with findings of other research groups, showing that increasing the viscosity will enhance the effect of contrast agents [45].

Furthermore, it was found that the bulk T_1-time lowers with decreasing the amount of glycerol, while the opposite happens with the bulk T_2-time. The increase of the T_2-relaxation time can be related to a decrease in diffusion when adding glycerol. In previous research, it was proven that with high gradients, the T_2-time can be approximated by $T_2 \approx 1/(\alpha\gamma^2 G^2 D t_e^2)$ [8]. Therefore, the increase in T_2 - time is a direct result of the effect of glycerol on the diffusion coefficient. An opposite behavior is observed for the T_1-relaxation time where increasing the viscosity will decrease the relaxation time in accordance with the Bloombergen-Purcell-Pound (BPP) theory [46]. In most studies, gadolinium-based contrast agents are tested in solutions mimicking blood plasma because of its medical applications. Most reported values are around 5 $ms^{-1}\,M^{-1}$ [44,47]. The result of normal water is quite close to the reported value, too be expected as blood plasma consists mostly of water.

When the relaxation parameters are known, a prediction of the signal intensity as a function of contrast agent can be made by implementing the values from Table 2 in eq. (4). Results of this prediction for the water-Clariscan mixture (0 wt% glycerol) are shown by lines in Fig. 6a. The colours are used to mark different repetition times. Furthermore, Fig. 6a shows experimental values measured by UFI (marked with dots). This graph shows that there is a good correlation between the prediction (based on the relaxation characteristics of the contrast agent) and the experimental results. Using the graph, the optimum Clariscan concentration can be determined for every desired repetition time. As found in section 3.4, lower repetition times results in lower maximum achievable signal intensity and an increase in contrast agent. Similar optimalization curves for all different mixtures can be found in Appendix B.

Fig. 6b shows the signal intensities for different water-glycerol contents, but for the same repetition time of 25 ms. For the same repetition time, the optimum concentration moves to the left with increasing glycerol content. As a consequence, a lower amount of contrast agent for higher glycerol contents is required to achieve optimal signal intensities.

Because the UFI-method relies on a short T_1-relaxation time, a contrast agent is mandatory in most liquids, as explained in Fig. 5. In this part, we showed that the method can be used for liquids with a wide variety of viscosity's. However, for low viscosity liquids with a high penetration speed, the method breaks down when no soluble contrast agent is available. This puts some limits on the types of liquids that can be used within our UFI-measurements.

4.2. Signal calibration in porous media

The main goal of UFI method is to measure liquid distributions in thin media on timescales as low as 10–100 ms. From eq. (5), it is known that $S \propto \rho$but also depends on T_1 and T_2. These relaxation times can be influenced by the porous media due to surface relaxation or reducing the

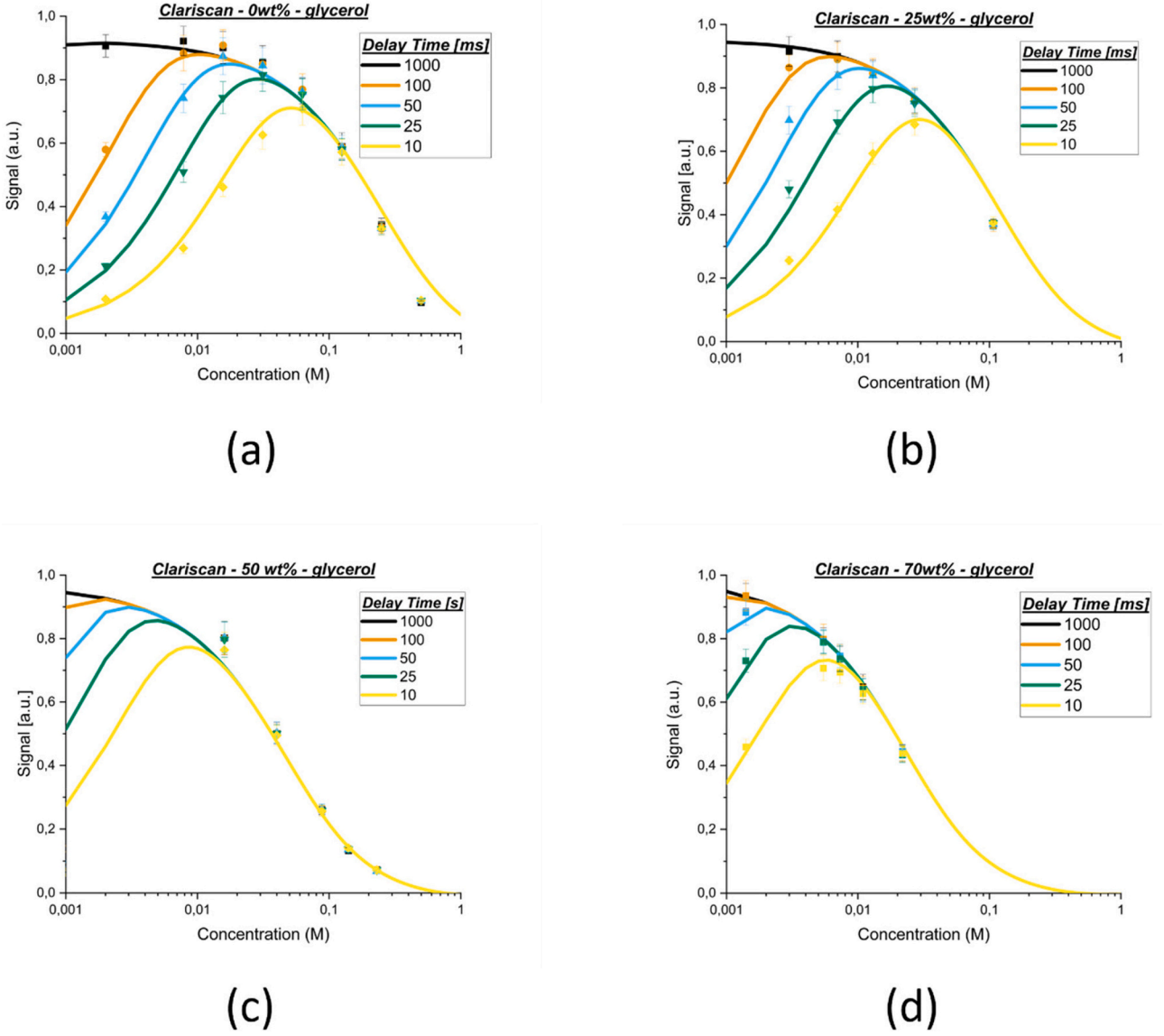

Fig. 15. Fast Sequence signal intensities data for CuSO4 containing solutions predicted by the contrast agent relaxivities (lines) and experimental results (points). The figures show the values for different glycerol contents (0 wt% (a), 25 wt% (b), 50 wt% (c) and 70 wt% (d)) where in every graph the values are given for different delay times: 1000 ms (black), 100 ms (orange), 50 ms (blue), 25 ms (green), 10 ms (yellow). (For interpretation of the references to colour in this figure legend, the reader is referred to the web version of this article.)

diffusion. These effect are well described by Brownstein and Tarr [48]. To test if the relaxation times depend on the nature of the porous media, relaxation times of typical solutions used in the fast sequence and demineralized water are determined in different porous media. The measured T_2 and T_1-relaxation times are shown in Fig. 7.

From these measurements, it is concluded that for normal water, the pore space influences the relaxation times and the resulting signal. The T_2- relaxation time for water increases with decreasing pore radius, which is the result of confining the hydrogen atoms and lowering the effective diffusion coefficient. This effect is clearly observable for demineralized water. In these measurements, the T_2-relaxation time was measured with an echo time of 50 μs. With a diffusion coefficient of $2.1{\cdot}10^{-9}$ m^2/s, this results in a diffusion distance of $\sqrt{2Dt_e} = 458$nm. If the pore radius is larger than the typical diffusion length, the relaxation behaves similar to that of a free solution, resulting in comparable relaxation times for free water and the once found in PVDF-0.65. For smaller pore radii, the diffusion distance will change to $\sqrt{2D_{eff}t_e}$ where D_{eff}depends on the pore space. The diffusion contribution to the relaxation time, will become less profound with higher concentrations of contrast agent. If one would compare the signal intensity of the CuSO4 0.2 M solution (T_2=6 ms) with the one found in PVDF 0.2 (T_2=7 ms), the signal measured by the fast pulse sequence would only increase from 0.875 to 0.89. This increase is only 1.5% and is much lower than the actual noise found within the system. Therefore it can be concluded that the pore radius will not influence the final signal intensity.

For the T_1-time, the pore space has a negative effect on the relaxation of normal water. An increasing surface to volume ratio means more surface relaxation and a lower relaxation time. From these measurements it can also be observed that PVDF has less surface relaxivity than Nylon, because for the same pore radius, the PVDF has a higher T_1-relaxation time. However when high amounts of contrast agents are used, the effect of the contrast agent is much more dominant and the relaxation time will be unchanged for the different pore spaces and solution.

Therefore, it can be concluded that the pore space will only influence the relaxation times for demineralized water. However, when contrast

agents are added, the effect of the contrast agent is much more dominant and the pore space has no significant effect on the final signal intensity. In case of our experiments, the amount of contrast agents is high enough to consider that the T_1 and T_2times are purely determined by the liquid properties and not by the porous matrix. Therefore, we take that any change in signal intensity can be related to a change in the hydrogen content (ρ).

4.3. Measuring liquid distribution profiles during imbibition

4.3.1. Ultra fast imaging of liquid profiles

Liquid penetration experiments were performed by jetting droplets on top of PVDF-membrane filters. After jetting, the UFI method is used to measure liquid distribution profiles during imbibition. By investigating the shape and position of the liquid front and the signal profiles, details of the fundamental processes can be obtained. Liquid distribution profiles of the Clariscan based mixture containing 50 wt% - glycerol from Table 1 penetrating inside a PVDF membrane with pore size 0.22 μm are plotted in Fig. 8a for different times during penetration. The signal intensity is given with respect to a fully saturated sample containing the same test liquid. The profiles are measured every 26.6 ms and are indicated with different colours. The black line with almost no signal is the signal intensity measured just before the droplet hits the membrane. By looking at the profiles, three different regions can be distinguished: the droplet on top of the substrate ($x < 0$ μm), the membrane ($0 < x < 165$ μm) and the glass plate (> 165 μm). Every region has its own signal intensity, the droplet with signal intensity 1, the membranes with signal intensity 0.65 and the tape with signal intensity 0. The droplet has a signal intensity of 1, meaning that the area is fully saturated with liquid. The membrane, however, has a maximum signal intensity of 0.65 indicated with a blue dotted line. Because the signal intensity is independent of the interaction between spins and the membrane, see section 4.2, the signal reflects the level of liquid saturation. If a fully saturated porous membrane is assumed, the final signal intensity reflects the porosity of the system which in this case corresponds to 0.65. This value is the same as the porosity measured by MIP which indicates that almost no air is trapped within the porous media after penetration. The profiles show that within PVDF membrane filters the liquid imbibes with a sharp front.

4.3.2. Liquid front penetration seen from profiles

Using these liquid profiles, a front position is taken at half the maximum signal intensity (0.33). The front positions for every liquid profile is marked in Fig. 8a with a square in the same colour as the corresponding liquid profile. In Fig. 8b, the front is plotted as a function of t where the same colours are used and where the straight line is drawn as guide to the eye. This plot shows that the penetration follows a linear time behavior which deviates from the earlier found results on Nylon 6,6 membranes that scaled with $\sqrt{t}$ [29].

4.3.3. Liquid penetration as function of pore radius and viscosity

To investigate the effect of viscosity, surface tension and pore radius, the experiment was repeated for all Clariscan based liquids containing different glycerol contents (Table 1) and different PVDF membranes. Fig. 9 shows the fluid front positions for all experiments. From this figure, it can be seen that the imbibition speed decreases with increasing glycerol content and with decreasing pore radius.

4.3.4. Comparing liquid penetration in Nylon and PVDF membranes

To compare the measurement on PVDF with earlier experiments on Nylon 6,6 membranes from reference [29], the data is plotted as function of $\sqrt{\sigma rt/\eta}$ in Fig. 10. The rescaling is based an a 1-D Darcy model, which predicts the fluid front position to be: $(l^2 = 4(K_0 cos(\theta)/\phi)(\sigma rt/\eta))$. In our previous article it was proven that in these particular systems, the penetration can be assumed to be 1D and that the model works for Nylon 6,6 membranes [29]. After rescaling, the Nylon and PVDF measurement follow two different master curves shown in red (Nylon) and blue (PVDF). In Nylon, penetration follows a square root of time behavior as predicted by Darcy, whereas PVDF does not. Kuijpers et al. observed a similar effect when measuring the absorption of water-glycerol mixtures in PVDF membranes with ASA [34].

A second observation drawn from the figures is that the penetration inside nylon membranes happens much faster. As the measurements are rescaled with $\sqrt{\sigma rt/\eta}$, the faster penetration cannot be linked to one of these parameters. Also both porosity's are quite similar, which was found by the NMR-profiles. Therefore, there should exist a difference in K_0 or θ between both membranes to explain the observed behavior. Possible reasons could be differences in fiber orientations or tortuosity [49].

4.4. ASA experiments

In the last section, the results found by the UFI are compared to ASA. Fig. 11 compares the NMR-data and ASA-measurements, where the NMR data is plotted in orange and the ASA data is plotted in green. The data is shown for both membranes (PVDF,Nylon) and for all glycerol contents (0, 25,50 and 70 wt%). ASA-measurements were performed using liquids with the same water-glycerol ratios, but without the contrast agent on both Nylon 6,6 membranes. Data for the PVDF membrane with a pore radius of 0.22 μm were taken from a previous study performed by Kuijpers et al. [34]. The NMR data for PVDF membranes are taken from Fig. 11 while the NMR data for the Nylon membranes are taken from our earlier work [29].

This figure shows that the measured liquid fronts for NMR and ASA are in good comparison, underlining again that both techniques show similar results.

5. Conclusion

In this paper an Ultra Fast Imaging (UFI) NMR method was introduced that is able to measure moisture profiles during imbibition with a temporal resolution of 10 ms and spatial resolution of 14.5–18 μm.

Before a liquid imbibition process can be measured, the signal intensity is optimized by the addition of a contrast agent. In this study two main contrast agents were studied, namely Clariscan and CuSO4. For both contrast agents, an optimum concentration could be determined with a theoretical model, which was based on the relaxation characteristics of the corresponding contrast agent. It was also shown that by the addition of those contrast agents, the measured signal intensity was independent of the porous medium and was fully determined by the hydrogen density.

After a clear characterization of the measured signal intensity, penetration experiments were performed on PVDF membranes with two different pore radii (0.22 μm and 0.65 μm). In the measured moisture distribution profiles the droplet, membrane and tape could be clearly distinguished. From the profiles, the porosity could be determined to be 65% which agreed well with porosity's measured by Mercury intrusion porosometry. The liquid distribution profiles in PVDF revealed a sharp moving liquid front, which could be used to measure the liquid front penetration speed for different water- glycerol mixtures and membrane pore radii. The liquid front penetration speed for the PVDF membranes showed to decrease with increasing viscosity and decreasing pore radii of the membrane. Different from previous measurements on Nylon 6,6 [29] the front position could not be rescaled with $\sqrt{\sigma rt/\eta}$. However a rescaling with $\sigma rt/\eta$ was possible. The deviation could not be related to the effect of swelling as was proposed by Kuijpers et al. [34]. However further research is required to explain this behavior.

Finally the NMR-measurements were compared to ASA measurements and showed good agreement. The advantage of the UFI NMR imaging method however is that a direct moisture profile within the

membrane can be measured. Being able to measure inside the media, allows to study more physical and chemical liquid uptake phenomenons, making the techniques much more valuable.

CRediT authorship contribution statement

R.J.K. Nicasy: Conceptualization, Methodology, Writing – original draft, Visualization, Investigation. **H.P. Huinink:** Conceptualization, Writing – review & editing, Supervision, Funding acquisition. **S.J.F. Erich:** Conceptualization, Writing – review & editing, Supervision, Funding acquisition. **O.C.G. Adan:** Conceptualization, Writing – review & editing, Supervision, Funding acquisition. **N. Tomozeiu:** Conceptualization, Writing – review & editing, Supervision, Funding acquisition.

Declaration of Competing Interest

None.

Acknowledgements

This publication is part of the project PQP (Print Quality and Particles) (Project No. 17099) of the research collaboration program High Tech Systemen en Materialen (HTSM) 2018 TTW, which was (partly) financed by the Dutch Research Council (NWO). The researchers would also like to thank H. Dalderop (TU/e) and M. Kurvers (TU/e) for helping to build the experimental setup. We acknowledge P. Lipman (TU/e) for doing the MIP measurements, H. Koier (CPP) for the viscocity and R. Vanos (CPP) for the surface tension measurements. Last we would like to thank Covestro and Canon Production Printing for their support.

Appendix A. Derivation of the Ultra Fast Imaging Sequence signal intensity

In this section, a detailed derivation is given of eq. (5). The derivation starts with eq. (4)

$$S = \rho\left(1 - exp\left(-\frac{t_r}{T_1}\right)\right)\sum_{n=1}^{2N} exp\left(-n\frac{t_e}{T_2}\right). \tag{8}$$

For simplicity, we set $x = t_e(1/T_2)$ and $y = \rho(1 - exp(t_r/T_1))$ which results in:

$$S = y\sum_{n=1}^{2N} e^{-nx}. \tag{9}$$

After rearrangement, this equation can be turned into:

$$S = y\left(\sum_{n=0}^{\infty} e^{-nx} - 1 - \sum_{n=2N+1}^{\infty} e^{-nx}\right). \tag{10}$$

When using the geometric series $\left(\sum_{n=0}^{\infty} exp(-n\alpha) = 1/(1-\alpha)\right)$ on the first term and replacing $n^{'} = n - (N+1)$ in the last term, we end up with,

$$S = y\left(\frac{1}{1-e^{-x}} - \frac{1-e^{-x}}{1-e^{-x}} - e^{-(2N+1)x}\sum_{n'=0}^{\infty} e^{-n'x}\right). \tag{11}$$

When again using a geometric series on the last term and doing some more calculations we end up with,

$$\begin{aligned} S &= y\left(\frac{1}{1-e^{-x}} - \frac{1-e^{-x}}{1-e^{-x}} - \frac{e^{-(2N+1)x}}{1-e^{-x}}\right), \\ S &= y\left(\frac{e^{-x} - e^{-(2N+1)x}}{1-e^{-x}}\right). \end{aligned} \tag{12}$$

By replacing x and $y$again, we end up with eq. (5):

$$S = \rho\left(1 - e^{-\frac{t_r}{T_1}}\right)\left[\frac{e^{-\frac{t_e}{T_2}} - e^{-(2N+1)\frac{t_e}{T_2}}}{1 - e^{-\frac{t_e}{T_2}}}\right]. \tag{13}$$

Appendix B. Contrast agent characteristics in different water-glycerol mixtures

In section 4.1, relaxation time measurements for different CuSO4 and Clariscan containing water/glycerol mixtures were introduced. Besides the relaxation times, also the signal intensity in function of the contrast agent was discussed and shown in Fig. 6 for a clariscan solution containing 0 wt% glycerol. In this appendix, graphs for the inverse T_1- and T_2- relaxation times are given in function of the $CuSO_4$ (Fig. 12) and Clariscan (Fig. 14) concentration. Also the remaining data showing the signal intensity for varying water/glycerol mixtures containing 0, 25, 50 or 70 wt% of glycerol are shown in function of the CuSO4 (Fig. 13) and Clariscan (Fig. 15) concentration.

References

[1] Noh H, Phillips ST. Metering the capillary-driven flow of fluids in paper-based microfluidic devices. Anal Chem May 2010;82(10):4181–7. https://doi.org/10.1021/AC100431Y/SUPPL_FILE/AC100431Y_SI_005.PDF.

[2] Songok J, Toivakka M. Controlling capillary-driven surface flow on a paper-based microfluidic channel. Microfluid Nanofluidics Apr. 2016;20(4):1–9. https://doi.org/10.1007/S10404-016-1726-1/FIGURES/10.

[3] Li B, Yu L, Qi J, Fu L, Zhang P, Chen L. Controlling capillary-driven fluid transport in paper-based microfluidic devices using a movable valve. Anal Chem Jun. 2017;89(11):5707–12. https://doi.org/10.1021/ACS.ANALCHEM.7B00726/ASSET/IMAGES/LARGE/AC-2017-00726T_0003.JPEG.

[4] Krainer S, Smit C, Hirn U. The effect of viscosity and surface tension on inkjet printed picoliter dots. RSC Adv 2019;9(54):31708–19. https://doi.org/10.1039/C9RA04993B.

[5] Waldner C, Mayrhofer A, Hirn U. Measuring liquid penetration in thin, porous sheets with ultrasound and drop absorption – scope and limitations. Colloids Surf A Physicochem Eng Asp Oct. 2022;650:129551. https://doi.org/10.1016/J.COLSURFA.2022.129551.

[6] Lamminmäki TT, Kettle JP, Gane PAC. Absorption and adsorption of dye-based inkjet inks by coating layer components and the implications for print quality. Colloids Surfaces A Physicochem Eng Asp May 2011;380(1–3):79–88. https://doi.org/10.1016/J.COLSURFA.2011.02.015.

[7] Baukh V, Huinink HP, Adan OCG, Erich SJF, Ven van der LGJ. Predicting water transport in multilayer coatings. Polymer (Guildf) Jul. 2012;53(15):3304–12. https://doi.org/10.1016/J.POLYMER.2012.05.043.

[8] Voogt B, Huinink H, Erich B, Scheerder J, Venema P, Adan O. Water mobility during drying of hard and soft type latex: systematic GARField 1H NMR relaxometry studies. Prog Org Coat Oct. 2018;123:111–9. https://doi.org/10.1016/J.PORGCOAT.2018.06.011.

[9] Morais FP, Curto JMR. Challenges in computational materials modelling and simulation: a case-study to predict tissue paper properties. Heliyon May 2022;8(5). https://doi.org/10.1016/J.HELIYON.2022.E09356.

[10] Gigac J, Fišerová M, Stankovská M, Maholányiová M. Prediction of water-absorption capacity and surface softness of tissue paper products using photoclinometry. O Pap 2019;80(08):91–7.

[11] Songok J, Salminen P, Toivakka M. Temperature effects on dynamic water absorption into paper. J Colloid Interface Sci Mar. 2014;418:373–7. https://doi.org/10.1016/J.JCIS.2013.12.017.

[12] Salminen P, Painola. Studies of water transport in paper during short contact times. Åbo: Laboratory of Paper Chemistry. Department of Chemical Engineering. Åbo Akademi. 1988.

[13] Washburn EW. The dynamics of capillary flow. Phys Ther Rev 1921;17(3):273–83. https://doi.org/10.1103/PHYSREV.17.273.

[14] Lucas R. Ueber das Zeitgesetz des kapillaren Aufstiegs von Flüssigkeiten. Kolloid-Zeitschrift 1918 231 Jul. 1918;23(1):15–22. https://doi.org/10.1007/BF01461107.

[15] Andersson J, Ström A, Gebäck T, Larsson A. Dynamics of capillary transport in semi-solid channels. Soft Matter Apr. 2017;13(14):2562–70. https://doi.org/10.1039/C6SM02305C.

[16] Schoelkopf J, Gane PAC, Ridgway CJ, Matthews GP. Practical observation of deviation from Lucas-Washburn scaling in porous media. Colloids Surf A Physicochem Eng Asp 2002;206(1–3):445–54. https://doi.org/10.1016/S0927-7757(02)00066-3.

[17] Terzis A, et al. Heat release at the wetting front during capillary filling of cellulosic micro-substrates. J Colloid Interface Sci Oct. 2017;504:751–7. https://doi.org/10.1016/J.JCIS.2017.06.027.

[18] Roberts R, Senden T, Knackstedt M, Lyne M. Spreading of aqueous liquids in unsized papers is by film flow. J Pulp Pap Sci 2003;29:123–31.

[19] MacDonald BD. Flow of liquids through paper. J Fluid Mech Oct. 2018;852:1–4. https://doi.org/10.1017/JFM.2018.536.

[20] Sarah K, Ulrich H. Short timescale wetting and penetration on porous sheets measured with ultrasound, direct absorption and contact angle. RSC Adv Apr. 2018;8(23):12861–9. https://doi.org/10.1039/C8RA01434E.

[21] von Bahr M, Seppanen R, Tilberg F, Zhmud B. Dynamic wetting of AKD-sized papers. J Pul Pap Sci Mar. 2004;30(3):74–81.

[22] P. Samyn, "Wetting and hydrophobic modification of cellulose surfaces for paper applications,"https://doi.org/10.1007/s10853-013-7519-y.

[23] Kuijpers CJ, Huinink HP, Tomozeiu N, Erich SJF, Adan OCG. Sorption of water-glycerol mixtures in porous Al2O3 studied with NMR imaging. Chem Eng Sci 2017;173:218–29. https://doi.org/10.1016/j.ces.2017.07.035.

[24] Perrin JC, Waldner C, Bossu J, Chatterjee A, Hirn U. Real time monitoring of the through thickness moisture profile of thin sheets using NMR. Chem Eng Sci Apr. 2022;251. https://doi.org/10.1016/J.CES.2022.117464.

[25] Mohebbi B, Tavangarrad AH, Claussen J, Blümich B, Hassanizadeh SM, Rosati R. Revealing how interfaces in stacked thin fibrous layers affect liquid ingress and transport properties by single-sided NMR. J Magn Reson Sep. 2018;294:16–23. https://doi.org/10.1016/J.JMR.2018.06.014.

[26] Tavangarrad AH, et al. Continuum-scale modeling of water infiltration into a stack of two thin fibrous layers and their inter-layer space. Chem Eng Sci Nov. 2019;207:769–79. https://doi.org/10.1016/J.CES.2019.07.001.

[27] Glover PM, Aptaker PS, Bowler JR, Ciampi E, McDonald PJ. A novel high-gradient permanent magnet for the profiling of planar films and coatings. J Magn Reson 1999;139(1):90–7. https://doi.org/10.1006/jmre.1999.1772.

[28] Nicasy R, Huinink H, Erich B, Olaf A. NMR profiling of reaction and transport in thin layers: a review. Polym. Feb. 2022;*14*(4):*798*. https://doi.org/10.3390/POLYM14040798.

[29] Nicasy R, Huinink HP, Erich SJF, Adan OCG. High-speed NMR imaging of capillary action in thin nontransparent porous media. Phys Rev E Oct. 2021;104(4):L043101. https://doi.org/10.1103/PhysRevE.104.L043101.

[30] Merbach A, Helm L, Toth É. The chemistry of contrast agents in medical magnetic resonance imaging: Second Edition. In: The Chemistry of Contrast Agents in Medical Magnetic Resonance Imaging: Second Edition, Feb. 18; 2013.

[31] myHealthbox. Clariscan 0,5 mmol/ml Oplossing voor | myHealthbox. https://myhealthbox.eu/nl/clariscan-05-mmol-ml-oplossing-voor-injectie/5135676; 2022 (accessed Mar. 08, 2022).

[32] G. P. Association. Physical properties of Glycerine and its solutions. New York: Glycerine Producers' Association; 1963.

[33] Bolden J, Corder Z, Higdon C, Miller C. Measuring Surface Tension Using the Pendant Drop Method. 2015. doi: 10675.2/552630.

[34] Kuijpers CJ, van Stiphout TAP, Huinink HP, Tomozeiu N, Erich SJF, Adan OCG. Quantitative measurements of capillary absorption in thin porous media by the automatic scanning absorptometer. Chem Eng Sci 2018;178:70–81. https://doi.org/10.1016/j.ces.2017.12.024.

[35] Anthony Bristow J. Liquid absorption into paper during short time intervals. Sven Pap 1967;70(19):623–9.

[36] McDonald PJ, Akhmerov A, Backhouse LJ, Pitts S. Magnetic resonance profiling of human skin in vivo using GARField magnets. J Pharm Sci 2005;94(8):1850–60. https://doi.org/10.1002/JPS.20401.

[37] McDonald PJ, Istok O, Janota M, Gajewicz-Jaromin AM, Faux DA. Sorption, anomalous water transport and dynamic porosity in cement paste: a spatially localised 1H NMR relaxation study and a proposed mechanism. Cem Concr Res Jul. 2020;133:106045. https://doi.org/10.1016/J.CEMCONRES.2020.106045.

[38] Erich SJF. NMR imaging of curing processes in alkyd coatings. Technische Universiteit Eindhoven; 2006.

[39] Markley JL, Horsley WJ, Klein MP. Spin-lattice relaxation measurements in slowly relaxing complex spectra. J Chem Phys Dec. 2003;55(7):3604. https://doi.org/10.1063/1.1676626.

[40] Ostroff ED, Waugh JS. Multiple spin echoes and spin locking in solids. Phys Rev Lett 1966;16(24):1097–8. https://doi.org/10.1103/PHYSREVLETT.16.1097.

[41] Blumich B. NMR imaging of materials. NMR Imag Mater Jan. 2010. https://doi.org/10.1093/ACPROF:OSO/9780198526766.001.0001.

[42] Wolf GL, Halavaara JT. Basic principles of MR contrast agents. Magn Reson Imaging Clin N Am 1996;4(1):1–10. https://doi.org/10.1016/S1064-9689(21)00550-X.

[43] Toth É, Helm L, Merbach AE. Relaxivity of MRI contrast agents. Berlin, Heidelberg: Springer; 2002.

[44] Rohrer M, Bauer H, Mintorovitch J, Requardt M, Weinmann HJ. Comparison of magnetic properties of MRI contrast media solutions at different magnetic field strengths. Invest Radiol Nov. 2005;40(11):715–24. https://doi.org/10.1097/01.RLI.0000184756.66360.D3.

[45] Kim TH. Pulsed NMR : Relaxation Times as Function of Viscocity and Impurities. 2008. p. 1–5.

[46] N. Bloembergen, *NUCLEAR MAGNETIC RELAXATION*, 1st ed. Dordrecht: Springer Dordrecht.

[47] Szomolanyi P, et al. Comparison of the relaxivities of macrocyclic gadolinium-based contrast agents in human plasma at 1.5, 3, and 7 T, and blood at 3 T. Invest Radiol Sep. 2019;54(9):559. https://doi.org/10.1097/RLI.0000000000000577.

[48] Brownstein KR, Tarr CE. Importance of classical diffusion in NMR studies of water in biological cells. Phys Rev A Jun. 1979;19(6):2446. https://doi.org/10.1103/PhysRevA.19.2446.

[49] Tomadakis MM, Robertson TJ. Viscous permeability of random fiber structures: comparison of electrical and diffusional estimates with experimental and analytical results. J Thermoplast Compos Mater 2005;39(2):163–88. https://doi.org/10.1177/0021998305046438.